Biomimetic, Programmable, and Part-by-part Maneuverable Single-body Shape Morphing Film

Yongrok Jeong[1, 2], Junseong Ahn[1, 2], Ji-Hwan Ha[1,2], Jiwoo Ko[1,2], Soon-Hyoung Hwang[1], Sohee Jeon[1], Munjeong Bok[1], Jun-Ho Jeong[1], Inkyu Park[2*]*

[1]Department of Nano Manufacturing Technology, Korea Institute of Machinery and Materials (KIMM); 156, Gajeongbuk-ro, Yuseong-gu, Daejeon, 34103, Republic of Korea.
[2]Department of Mechanical Engineering, Korea Advanced Institute of Science and Technology (KAIST); 291, Daehak-ro, Yuseong-gu, Daejeon, 34141, Republic of Korea.
 Email: jhjeong@kimm.re.kr (Jun-ho Jeong), inkyu@kaist.ac.kr (Inkyu Park)

Recently, shape morphing films (SMFs) have been actively researched owing to their diverse applications such as soft robotics, soft gripper, and healthcare/wearable devices. Their complex movements have been typically made by assembling multiple actuation elements in a single system. However, the unreliability during assembly process has been a critical issue, which has restricted their practical usage. In order to resolve this problem, this study proposes a biomimetic, programmable, and part-by-part maneuverable single-body SMF. Programming of the SMF adopts a similar mechanism to *Bauhinia variegates,* whereby nonequivalent volume changes due to external stimuli cause the bending of the overall film. The patterned elastic modulus of the SU-8 micro-wall prescribes the preferred bending direction. Part-by-part maneuvering is accomplished by controlling the voltage distribution of the underlying electrothermal heater. The fabricated single-body SMF demonstrates the complex movements of the inchworm (pose stabilization: front-to-back flip and back-to-front flip; basic movements: crawl, left turn, and right turn) and *Drosera Capensis* (insect-gripping via hierarchical morphology). The proposed method for the fabrication of a biomimetic, programmable, and part-by-part maneuverable single-body SMF can successfully replace the conventional assembly process and achieve advanced SMF technology by enabling various complex movements towards practical applications.

1. Introduction

Recently, shape morphing films (SMFs) have been widely researched because of their diverse potential applications, including soft robotics, [1–7] soft grippers [8–12], and healthcare/wearable devices [13–15], and compatibility with conventional 2D fabrication processes [16]. Recent research about SMF concentrates on improving the morphing complexity, which is determined by the morphable shapes and their arrangements. For this purpose, two critical features need to be improved: part-by-part maneuvering and part-by-part programming. With these features, SMF can be partially and independently morphed, and this helps to achieve the higher morphing complexity. Especially, part-by-part maneuverability has been realized by two methods: multi-responsive SMF and assembly of multiple components in a single system. In the first method, the SMF is composed of multiple components, which respond to different types of physical stimuli (eg. light, magnetic field, humidity, temperature, etc.[17]), and they can be independently controlled to enable a complex shape morphing such as the crawler with part-by-part actuation [1,5,9,10,12,18–20]. However, this method has intrinsic limitations: restricted environmental parameters and morphing degree of freedom (DOF). Shape morphing necessitates a control of multiple environmental factors, and thus their working environment is highly restricted [3,8,21,22]. Furthermore, the number of the independently morphable region is restricted by the number of different stimuli, which is insufficient for the highly complex shape morphing. In contrast, the second method based on the assembly of multiple components in a single system enables selective movement of each element such as the realization of wing actuation of a bird in-flight [23], and thus it is less restricted by environmental parameters and allows for nearly unlimited morphing DOF in theory [7,11,24]. However, most of them are manually assembled, leading to unreliability in the assembled result, and are unsuitable for complex movements such as the gripping motion of the *Drosera Capensis,* which needs elaborate morphology and a highly ordered structure with multiple parts. In summary, complex movements are hard to be realized with the present technologies. In the present work, the proposed method solves the aforementioned problems by fabricating a biomimetic, programmable, and part-by-part maneuverable single-body SMF. It is intended as a replacement for conventional assembly methods and has been successfully adopted in an SMF that imitates complex movements observed in nature. Programming of the SMF involves a mechanism similar to that of the *Bauhinia variegates*: The hygroscopic volume change of overall tissue was restricted in a predefined direction by the cellulose fibril structure, thereby causing the overall tissue's bending in the intended direction. Similarly, the temperature-induced volume changes and elastic modulus patterning-based restriction in

morphing direction cause the bending of the overall film in the intended direction [26]. The patterned elastic modulus of the SU-8 micro-wall prescribes the preferred bending direction of the SMF. The shape of the SU-8 micro-wall is optimized to maximize the bending curvature. Part-by-part maneuvering is accomplished by controlling the voltage distribution of the embedded electrothermal heater. Finally, the fabricated single-body SMF imitates the complex movements of an inchworm (pose stabilization: front-to-back flip and back-to-front flip; basic movements: crawl, left turn, and right turn) and *Drosera Capensis* (insect-gripping via hierarchical morphology). The motion of the artificial inchworm is enabled by both part-by-part programmable and part-by-part maneuverable features, whereas the motion of the artificial *Drosera Capensis* is realized by the fabrication of hierarchical morphology (mm-cm scale).

2. Results and Discussion

2.1. Principle

In nature, certain tissues undergo anisotropic morphing in response to changes in their environment [27–30]. This behavior is a result of both nonequivalent volume change and a patterned elastic modulus (E). For example, the seedpod of *Bauhinia variegates* morphs in a chiral geometric pattern due to a change in the volume of individual tissues induced by change in humidity (nonequivalent volume change) and the periodic cellulose pattern inside the seedpods (patterned E) [26]. Analogous to this, the morphing behavior of the shape morphing module is driven by the difference in the coefficients of thermal expansion (CTE) between the constituent polymers (nonequivalent volume change), and by patterned E through the internal SU-8 microstructures. The polyimide (PI) substrate, which has a low CTE (38 ppm) and high E (2.52 GPa), is micro-patterned with SU-8 [31], which also has a low CTE (50 ppm) and high E (4.95 GPa), resulting in a PI/SU-8 complex with similar physical properties (CTE and E). Polydimethylsiloxane (PDMS), which has a high CTE (340 ppm) and low E (0.0067 GPa), is coated on the patterned substrate. Because PDMS has a much higher CTE and lower E than PI and SU-8, it can induce a volume change while minimally affecting the patterned E. Structurally, the SU-8 micro-walls are soaked with PDMS, resulting in a robust mechanical interlocking between the PI and PDMS layers with strong adhesion between them. In the perpendicular orientation to the SU-8 microwalls, the bending modulus of the PI/SU-8 complex is maximized, and the bending in the perpendicular direction is suppressed. By contrast, in the parallel orientation to the SU-8 microwalls, the bending modulus of the PI/SU-

3

8 complex is comparatively smaller, and thus the bending in the parallel direction is preferred. The bending orientation is thus imposed by the structure of the PI/SU-8 complex (**Figure 1A**). In addition to the shape-morphing module, the proposed system contains an electrothermal heater (Figure 1B). The electrothermal heater elevates the temperature of the target region, and the shape morphing module induces the morphing of the film. In the electrothermal heater, a nichrome (NiCr) nano-mesh structure is embedded between PI layers by the methods presented in a previous paper (**Figure S1A**). The interconnection for voltage input is patterned onto the NiCr nano-mesh, depending on the areas for individual heating control. Various voltage distributions made from multiple interconnections maneuver individual parts of the SMF (Figure 1C). The heating/cooling of the heater can be determined by the voltages of two nodes at each end of the heater. If the voltages at two nodes are different ($|V_{left} - V_{right}|$ = $|\Delta V| > 0$), this area is heated. On the other hand, if the voltages at two nodes are the same ($V_{left} - V_{right} = \Delta V = 0$), this area is not heated. For example, two types of stepping-stone mode of heating for five-nodes heater are depicted in Figure 1C. In the first example (Figure 1C-i), the regions #1 and #3 are heated because of the voltage difference between the nodes #1 and #2 ($V_1 \neq V_2$), and that between the nodes #3 and #4 ($V_3 \neq V_4$). In the second example (Figure 1C-ii), the regions #2 and #4 are heated in a similar manner because of the voltage differences between the nodes #2 and #3, and that between the nodes #4 and #5. By controlling a proper sequence for the node voltages, part-by-part maneuvering of the SMF is realized. SU-8 is patterned on the fabricated heater by a conventional lithography process used in micro-structuring (Figure S1B), and PDMS is conformally coated on it using roll imprinting followed by spin coating (Figure S1C). On the fabricated sample, electrical contact areas on the PDMS are first opened, and then the whole sample is released from the wafer (Figure S1D). Finally, using the part-by-part maneuverable SMF, the complex motions of the inchworm and *Drosera Capensis* are imitated (Figure 1D).

2.2. Optimization and Characterization of the Shape Morphing Module

The bending curvature of the shape morphing module was optimized using a grid selection method based on simulation results (**Figure S2**) to select the width (w), pitch/width ratio (p/w), height (t_{SU-8}) of the SU-8 micro-wall, and the relative thickness of PDMS with respect to that of SU-8 (t_{PDMS}/t_{SU-8}). The change in the numerically calculated curvature (κ) between the initial and heated states was selected as the criterion for the comparison of the results. Four options were investigated for each factor (w, p/w, t_{SU-8}, and t_{PDMS}/t_{SU-8}), generating a total of 256 results (4^4) (**Figure S3**). The top 20 results are depicted in **Figure 2A**. The results

show that curvature reaches a maximum at $w = 25$ μm, $p/w = 2$, $t_{SU-8} = 75$ μm, and $t_{PDMS}/t_{SU-8} = 1.5$. Moreover, the same variable values result in the desired morphing of the film in the forced orientation: $\kappa_1 \sim 0$ (i.e., no bending) for the orientation perpendicular to the micro-wall pattern, and $\kappa_2 > 0$ (i.e., bending) for the orientation parallel to the micro-wall pattern. The fabrication variables were set to optimized design values based on the simulation results (Figure 2B-C). The resulting structure entails a NiCr nano-mesh pattern with width = 130 nm, pitch = 920 nm, and height = 48.2 nm fabricated uniformly between two PI layers (Figure 2B, C-iii). The shape morphing module with $w = 25.1$ μm, $p/w = 1.99$, $t_{SU-8} = 80$ μm, and $t_{PDMS}/t_{SU-8} = 1.28$ was then fabricated over the NiCr nano-mesh-embedded PI film (Figure 2C). This result agrees well with the optimization result and was thus selected as the fabrication condition for the SMF used hereafter.

To confirm that the proposed shape morphing module can be designed by the shape of the film and the orientation of the pattern, film samples were cut into various shapes and orientations and tested in a convection oven for a uniform temperature change (**Figure 3A**). A right-angle triangle, circle, and rectangles with various aspect ratios (49:1, 7:1, 1:1, 1:7, and 1:49, where x:y denotes the ratio of the length of the entire film perpendicular to the micro-wall pattern to that of the entire film parallel to the micro-wall pattern) were tested at temperatures between 25 °C and 150 °C. Figure 3A shows that all shapes at various orientations were clearly morphed to a pre-designed orientation with heating and cooling (the red arrow denotes the SU-8 wall direction of each SMF). Additionally, to confirm the independence of the orientation of the film from the shape of the SMF, samples of the same rectangular shape (1 ×40 [mm]) with a variety of SU-8 wall orientations (from 0 ° to 90 ° with respect to the long side of the rectangle, with an increment of 15 °), were tested (Figure 3B). Although all the SMFs have the same shape, the morphing orientation of the film successfully adopted the pre-designed orientation. In conclusion, the shape-morphing module can be designed by the shape of the film and the orientation of the pattern independently.

The results also contribute to the analysis of the relationship between the shape and orientation of the SMF and the consequent curvature. The shape of the SMF and orientation of the SU-8 micro-walls determine the required number of walls in the SMF to accomplish the final curvature. The relationship between the theoretical turn factor (r), representing the number of SU-8 micro-walls in a single SMF, and the measured turn number (n), representing the final curvature is plotted in Figure 3C. A linear relationship between r and n confirms that the curvature of the SMF after heating is dependent on both the shape and orientation of the

SMF. Details on the determination of r can be found in the supporting information (section: "Calculation of the theoretical turn factor").

To confirm the relationship between the ambient temperature (T) and the curvature of the electrothermal SMFs (κ), simulations at various T with respect to flat state (from -100 °C to 100 °C, with an increment of 20 °C) with the same geometrical model were conducted (Figure 3D). From this simulation, a linear relationship between normalized curvature (κ/κ_{max}) and temperature change (ΔT) was evident, with a constant coefficient of 0.046 [cm^{-1} °C $^{-1}$] (Figure 3E). The curing temperature (T') of PDMS also affects the range of curvature. A change in T' causes the thermal expansion/shrinkage of the PDMS precursor during the PDMS curing process and induces an offset in the curvature range. Figure 3E shows that the shape morphing module with PDMS cured at 200 °C has a smaller (negative) curvature, compared to that with PDMS cured at 50 °C, at the same ambient temperature. Quantitatively, a 50 °C increase in T' corresponds to a decrease of ~2.5 cm^{-1} in initial κ. During experimentation, it was found that $T' = 100$ °C is the optimal condition for bidirectional bending, the value applied to further experimentation. The two linear relationships ($\kappa - T, \kappa - T'$) can be combined to form a single linear relationship ($\kappa - T, T'$) as follows:

$$\kappa = 0.046T - 0.056T' + 2.034$$

The measured and calculated curvatures were compared (**Figure S4**). The mean absolute error (MAE) and R^2 were used to quantify error and uncertainties. MAE is calculated as follows:

$$MAE = \frac{1}{N} \sum_{i=1}^{N} |y_i - \widehat{y_i}|$$

where y_i denotes the real value and $\widehat{y_i}$ denotes the fitted value, for the result #i for N samples. The fitted result shows a MAE of 0.40 cm^{-1}, which is 2.83 % of the whole curvature range of the dataset (-7.89 ~ 6.18 cm^{-1}), with R^2 of 0.99, both of which are acceptable.

2.3. Characterization of the Shape Morphing Film

Prior to morphing, the thermal characteristics of the NiCr nano-mesh-based electrothermal heater were investigated by relating the power density P' (= Power/Area [W/cm^2]) to the corresponding temperature rise. The fabricated electrothermal heater exhibits a stable response at a temperature of 225 °C and $P' = 1$ W/cm^2 (**Figure S5C**) and a linear ΔT-P' relationship (Figure S5D, R^2 = 0.98). Moreover, it exhibits almost uniform heating, with a maximum standard deviation of 4.86% (Figure S5E-iii) according to the IR imaging results.

This method facilitates the fabrication of the mm-scale SMF because the fabrication of the proposed SMF primarily comprises lithography processes. In this study, two samples of sizes 1×1 and 5×5 mm^2 (Movies S1 and S2) were fabricated and analyzed. The first experiment investigated the change in κ with a change in P' (**Figure 4A**). The results show a linear relationship between P' and κ ($\kappa \propto P'$) for both samples. P' and ΔT of the heater are intrinsically linearly related ($P' \propto \Delta T$), and ΔT and κ are linearly related as per the numerical simulation results ($\Delta T \propto \kappa$). The experimental result agrees well with the theory. Another parameter used to characterize the SMF is the sensitivity, $S = \Delta\kappa/\Delta P'$. The results show that the 1×1 SMF possesses a higher sensitivity (*S*) of 7.83 cm/W than the 5×5 SMF, with a sensitivity of 6.26 cm/W. This difference can be attributed to the difference in the mass of the film. Being heavier, the 5×5 SMF is more affected by gravity, which counters bending.

In the second experiment, 10–90% rise time (τ_R) and 90–10% fall time (τ_F) were measured for $P' = 0.6$ W/cm^2 (Figure 4B). The results were $\tau_R = 4.08$ s, $\tau_F = 4.09$ s for the 1×1 SMF, and $\tau_R = 4.91$ s, $\tau_F = 11.11$ s for the 5×5 SMF. The large difference in τ_F can be attributed to the cooling mechanism of the SMF, which depends on convection through ambient air, and conduction through the interconnections. Finally, 1000 cycles of repeated heating/cooling tests were performed using a 5×5 SMF (Figure 4C). No noticeable irregularity in the curvature was observed during the 1000 heating/cooling cycles.

To investigate the robustness of programmability, 4×52 mm^2 belt-shaped SMF with various orientations were fabricated and characterized (Figure 4D, Movie S3). The movement of each belt followed the programmed direction, particularly in the negative curvature range ($P' = 0$ W/cm^2). By comparison, the positive curvature range ($P' = 0.6$ W/cm^2) showed relatively less movement response in the programmed bending direction. This may be attributed to the inability of the SU-8 micro-wall to completely restrict the expansion of the PDMS perpendicular to the micro-wall direction of SU-8 in the positive curvature range. The results were an offset in the range of curvature with repetitive heating and cooling. However, with sufficient aging, a steady range of curvature can be maintained (**Figure S6**). In later experiments, the negative curvature region was adopted as the main morphing range.

2.4. Complex Movements by Part-by-Part Maneuvering of Shape Morphing Film

To demonstrate part-by-part maneuvering, we imitated the inchworm for biomimetic crawling and the *Drosera Capensis* (Cape sundew) for biomimetic gripping. Detailed driving mechanisms are presented below.

Crawler: Artificial Inchworm

The inchworm is composed of two moving elements: the foot and the leg. Its foot selectively adheres to the ground, and the leg moves its entire body by bending. In this study, we imitated two features of the inchworm: selective adhesion of the foot and movement by bending of the leg. Selective adhesion was achieved using the difference in friction between PI and PDMS, and the bending motion was simulated by utilizing differently programmed multiple SMFs in a single soft robotic system. A single soft-robotic system with five SMFs was successfully fabricated (Fig 5A). This system consisted of the feet (A_1 and A_5) and legs (A_2–A_4). Six integrated interconnections (V_1–V_6) were placed to individually control the five SMFs (A_1–A_5) (**Figure S7**).

To enable the bi-morph feature of the foot with the same voltage difference that is needed to flatten the leg, the length of each foot was less than that of each leg. This made the resistance of the foot smaller than that of the leg, and the resulting power density of the foot greater than that of the leg. Consequently, the curvature change of the foot was larger than that of the leg, allowing both the PI and PDMS parts to selectively touch the ground. The difference in friction between the parts resulted in alternative anchoring (PDMS side) and releasing (PI side).

The orientations of the A_2 and A_4 legs were slanted and mutually opposed to enable bi-directional change in the crawling direction. Being the primary leg, the bending orientation of A_3 was designed perpendicular to the length direction of the system. In later experiments, the direction of movement for the artificial inchworm was set as follows: the front side denotes the state where the PI side is on top (**Figure 5A**, inset) and the forward direction denotes the direction from A_1 to A_5.

The first experiment studied pose stabilization by adopting two movements: the front-to-back and back-to-front flips. For the front-to-back flip (Figure 5B-i, Movie S4), one side of the leg (A_2) rolled under the artificial inchworm while the other leg parts (A_3–A_4) were flattened to prevent the flipping of the entire system (2nd step). Next, the foot at the rolled side (A_1) was heated to prevent additional rolling of the leg (3rd step). After foot anchoring at A_1, sequential rolling of the A_2-A_3-A_4 parts was performed (3rd–6th step), and finally, the whole system was flipped from the front to the back (7th step). By comparing the first and final figures in Figure 5B-i, it can be seen that the order of the SMF parts changed from A_1–A_5 to A_5–A_1, indicating a successful flip. Each step was observed using an IR camera, and it was confirmed that the heating and cooling states of the individual SMF parts occurred as intended. The heating of A_5 at the 4th step was performed to prevent the unintentional jamming of A_5 by altering its

curvature to convex relative to the SMF body. For the back-to-front flip (Figure 5B-ii, Movie S5), the entire artificial inchworm was folded in half by rolling (1st–3rd step), and the forelegs (A_4–A_5) were flattened to stabilize the front half while the rear half rolled under it (A_1–A_2) (4th–6th step). Like the front-to-back flip, each step was observed using an IR camera, and it was confirmed that the individual parts of the SMF operated as intended. These results confirmed that the proposed artificial inchworm can stabilize its pose without any external force. Detailed conditions for voltage regulation are shown in Figure S7A.

The second experiment demonstrated three basic movements: crawling, left turn, and right turn. For the crawl (Figure 5C-i, Movie S6), two legs (A_2, A_4) were flattened to maximize the moment arm of the artificial inchworm, two feet (A_1, A_5) were alternatively anchored on the ground by repetitive heating and cooling, and the mid-leg (A_3) accomplished the crawl action. When the rear foot (A_1) was anchored, the mid-leg (A_3) was flattened, and the entire body moved forward (1st–2nd step). Alternatively, when the front foot (A_5) was anchored, the mid-leg (A_3) was bent, and the entire body also moved forward (3rd–4th step). For the left turn (Figure 5C-ii, Movie S7), the left-oriented leg (A_2) was used for the primary movement while the other legs (A_3, A_4) prevented unintentional flipping of the body. When the left-oriented leg was rolled under the body, the front foot (A_5) was anchored to prevent the entire body from turning right (1st–2nd step). Next, the front foot was detached to prepare for the turning (3rd step), and the flattening of the left-oriented leg resulted in the body turning left (4th step). The same process was repeated for the right turn. The symmetry of the entire artificial inchworm during the turn was maintained with respect to the mid-leg (A_3), and only the heated/cooled state of the symmetric module (A_2–A_4, A_1–A_5) was changed (Figure 5C-iii, Movie S8). Detailed conditions for voltage regulation are shown in Figure S7B. The speed of the crawl and, left and right turns were observed for four cycles (**Figure S8A**). The results show a crawling speed of 0.125 mm/s and turning speeds of 0.123 and 0.148 °/s to the left and right, respectively (Figure S8B).

Gripper: Artificial Drosera Capensis

Drosera Capensis comprises two moving elements: the stem and leaves. The stem supplies the force to catch the target insect, and the leaves enable conformal contact with the target to prevent its escape. To achieve this, the leaves are composed of many cilia-like structures, capable of motion in a direction perpendicular to that of the stem. **Figure 6A-i** shows the fabricated artificial *Drosera Capensis* with a single planar actuator (length = 60 mm, width = 10 mm) that has a perpendicular bending direction with the electrode as a mimicry of stem and many cilia-like structures (length = 1 mm, width = 10 mm for each cilium) that have a

parallel bending direction with the electrode as a mimicry of leaves. For part-by-part maneuvering of the artificial *Drosera Capensis*, the voltage lines (V_1–V_4) are placed at the boundary lines of the stem and leaves. For the individually-morphed cilia structure, the end-part electrode of the cilia (V_1) also should be connected via the cilia itself, and thus the insulation between NiCr nanomesh and the electrode film should be formed. For the insulation, SiO_2 insulating layer was inserted between the NiCr nanomesh and the electrode film (Figure 6A-ii). In addition, the change in direction of the SU-8 microwall can be observed at the boundary of the leaf and stem.

Similar with the artificial inchworm, artificial *Drosera Capensis* can also be maneuvered in part-by-part (Figure 6B). Before heating, it is rolled in pill-like morphology, with a voltage profile of $(V_1, V_2, V_3, V_4) = (0, 0, 0, 0)$ (Figure 6B-i, Figure 6C - Initial position). By part-by-part maneuvering of stem part only, the planar actuator at the center is heated and unfurled, with a voltage profile of $(V_1, V_2, V_3, V_4) = (0, 0, V, V)$ (Figure 6B-ii). In addition to the previous state, a single left side of the leaf can be independently heated and unfurled, with a voltage profile of $(V_1, V_2, V_3, V_4) = (0, V, 0, 0)$ (Figure 6B-iii). In a similar manner, the whole SMF can be also heated and unfurled, with a voltage profile of $(V_1, V_2, V_3, V_4) = (0, V, 0, V)$ (Figure 6C - Ready to catch state). Controlling the voltage distribution enables not only part-by-part maneuvering, but also the maneuvering of different morphologies at the same temperature. Because the voltage differences between electrodes are the same for every composing SMF while the sheet resistance and the length between electrode are the same, the power density P' is the same for every part of the SMF. Thus, the whole artificial *Drosera Capensis* can be heated and unfurls by similar degrees, as can be seen in Figure 6C - Ready to catch state.

Fabricated system was applied to mimic the insect-gripping motion of the *Drosera Capensis*. Initially, the artificial *Drosera Capensis* is in a rolled state, which has a pill-like morphology (Figure 6C, Movie S9). After uniform heating of the entire SMF (~30 s), it unfurls, signaling readiness to catch the insect. Application of the voltage profile achieved uniform heating of the entire SMF, along with similar curvatures of the stem and leaves. When an artificial fly was placed on the artificial *Drosera Capensis* in its ready-to-catch state, it rolled-back to its initial state within 10 s, and snap-caught the fly. During this step, the cilia-like leaf structure conformed to the shape of an artificial fly (Figure 6C, encircled region in red dot).

3. Conclusion

The assembly of multiple pre-programmed SMF's into a single system is one approach to fabricating a flexible and complex shape morphing system, but it is still insufficient to successfully realize the complex movements due to the unreliability issues during the assembly process. To address these shortcomings and to present a novel solution for complex movements, a new way to fabricate a biomimetic, programmable, and part-by-part maneuverable single-body SMF with complex movement capability was presented in this work. Part-by-part programmability is achieved by a multi-layer structure with various CTE and *E*, similar with the seedpod of *Bauhinia variegates*. Nonequivalent volume expansion due to CTE differences in the constituent materials causes the bending of the overall film, and patterned *E* determines the bending orientation. Part-by-part maneuverability is realized by controlling the voltage distribution of the individual electrothermal heaters. Complex movements were demonstrated for two biomimetic applications: artificial inchworm (crawler) and artificial *Drosera capensis* (gripper). The respective applications demonstrate the effectiveness of the proposed method. For the artificial inchworm, both part-by-part maneuvering and part-by-part programming are required for individual modules to ensure smooth flipping or turning motions. For *Drosera capensis*, in addition to part-by-part programmability, a hierarchical morphology (mm-cm scale) is required to ensure uniform heating. Moreover, the cilia-like structures in this application have a width of 1 mm, which is extremely difficult to achieve via a conventional assembly process. In summary, part-by-part programming and maneuvering in complex morphology, even for hierarchical morphology, can be achieved using the proposed method. Although only relatively simple movements on mm-cm scale were demonstrated in this research, more complex movements can be achieved by the proposed method, because the lithographic method allows for finer patterning. Up to our knowledge, the proposed method is the most precisely programmable and freely maneuverable method to fabricate and control the elaborate shape morphing film (Table S1). Although, this method has significant advantages, there is scope for improvement. Firstly, only the bending deformation of the film has been investigated. By selecting materials with high difference in *E*, the effect of strain was made negligible. However, further applications may be possible by actuating not only a bendable but also a stretchable film with a similar strategy. For example, by selecting two materials with different CTE and similar *E* and arranging them in a circular wall pattern, the expansion of the overall structure may be possible, which can be applied to the imitation of the eye structure of a bug or an adaptive lens [32]. Secondly, a relatively simple voltage distribution was adopted in this research.

Complex voltage distributions can improve the complexity of the shape morphing and corresponding motions.

The proposed method for the fabrication of a biomimetic, programmable, and maneuverable single-body SMF can successfully replace the conventional assembly-based fabrication process. In addition, owing to the lithographic nature of the overall patterning process, it can be used in the fabrication of SMFs with various morphologies since fine patterns can be made easily. The SMFs can be custom designed using the proposed method, even for applications that require complex movement, and the technology can be applied as a solution to real-world problems.

4. Methods

Material selection

The most important factor in achieving biopolymer bending actuation is the CTE difference between the materials. To achieve sufficient flexibility, polymer-based materials are required for the fabrication of SMFs. Two of the most common pairs of polymers were used: PI (VTEC, PI-1388) and PDMS (Dow Corning, Sylgard 184). The material for elastic modulus patterning must be easy to shape, has similar E with PI, and have a low CTE. SU-8 (Microchem, SU-8 100), one of the most popular patternable epoxy materials, was selected for this purpose. SU-8 provides sufficient adhesion with PI after the hard-baking process without additional processing. To focus the power consumption at the heater layer, a large difference in conductivity is required between the heater and interconnections. Nano-mesh-patterned NiCr was selected as the heater layer, and Ag as the interconnection layer. The artificial Drosera Capensis requires an insulating layer between the heater and interconnection; thus, the SiO_2 film was deposited as an insulator.

For the artificial inchworm, ultra-thin Cu wires (AWG 45) were soldered onto the interconnection layer for electrical connection. For stability, an additional Au layer was deposited on the Ag to prevent the oxidation and sulfurization of the deposited Ag film. In summary, the SMF structure used is PI/NiCr(/SiO$_2$)/Cr/Ag(/Au)/PI/SU-8/PDMS.

Optimization of the SU-8 pattern

Optimization of the SU-8 pattern was conducted using commercial simulation software (COMSOL Multiphysics). The details of the simulation can be found in Figure S2. The optimal values for w, p/w, t_{SU-8}, and t_{PDMS}/t_{SU-8} were determined from the simulation and used in the fabrication of the SMF. Material selection was based on the CTE and E values (PI, SU-8, PDMS). Ten SU-8 micro-walls were incorporated into a single module, while $0.5(p-w)$ was spaced at the edge of each wall. In addition, wall length was made equivalent to the total module length (10 SU-8 walls). The resulting square SMF with a length of $10p$ was constructed.

Four constraints were preset: the movement of one corner was fixed ($dx = dy = dz = 0$), the adjacent two corners were restricted to a single direction that was parallel to the boundary of the reconstructed SMF ($dx = dz = 0$ and $dy = dz = 0$), and the non-adjacent corner was restricted only to z-direction movement ($dz = 0$). As a result, the SMF moved freely while maintaining the same z-level (Figure S2A). Next, the temperature of the simulated module was increased to 200 °C. The thermal expansion module of COMSOL was used to simulate

the thermal expansion and subsequent bending of the proposed SMF. Due to the patterned elastic modulus of the SU-8 wall, the film bent in a direction perpendicular to the SU-8 wall. The bending curvature of the center line was calculated, as shown in the supporting information (Figure S2A-iii) and adopted as the ranking criterion for the investigated conditions (Figure S3).

Fabrication of the SMF

Polyamic acid (PAA), the precursor of PI, was coated on a 4" Si wafer (spin coat: 3000 rpm, 30 s / soft bake: 150 °C, 1 min). The NiCr nano-mesh was then transferred onto the coated PAA. A custom-built roll imprinter was used for the transfer at 170 °C for 5 min (Figure S1A-ii). The detailed process of the NiCr nanomesh transfer can be found in a previous paper [33]. After the NiCr nano-mesh transfer, thermal imidization of the PAA was conducted at 270 °C for 1 h (Figure S1A-iii).

For the artificial *Drosera Capensis*, an additional insulator was inserted between the heater and the interconnection layer. The SiO_2 insulator was deposited by means of E-beam evaporation (200 nm with a deposition speed of 0.5 nm/s) and a lift-off method (Figure S1A-iv). AZ5214E was used as the photoresist for the lift-off layer. The lift-off pattern was fabricated using the conventional reversal baking process of AZ5214E (spin coat: 1000 rpm, 30s / soft bake: 112.5 °C, 1 min / Exposure: 40 mJ/cm^2 / post exposure bake (PEB): 122.5 °C, 2 min / develop: 2 min in AZ300 MIF solution). The bake temperature is higher than the original condition, and it is the result of the empirical calibration of the effect of the thermal resistance of the polyimide.

The interconnection was then deposited by E-beam evaporation and lift-off method (Cr/Ag, Cr 30 nm with a deposition speed of 0.2 nm/s, Ag 1000 nm with a deposition speed of 1 nm/s) (Figure S1A-v). After the fabrication of the electrothermal heater, the entire heater was covered with PI (spin coat: 3000 rpm, 30 s / soft bake: 150 °C, 1 min / full imidization: 260 °C, 1 h) (Figure S1B-i) with the exception of the parts intended for later electrical connection. These parts were masked with PI tape during the spin-coating process.

To cover the PI layer, the SU-8 photoresist was coated and patterned (spin coat: 3000 rpm, 30 s / flattening: 67.5 °C, 10 min / soft bake: 97.5 °C 30 min / exposure: 50 s / PEB: 97.5 °C, 10 min/develop: 5 min in SU-8 developer×, 4 times) (Figure S1B-ii). To fabricate the SU-8 micro-wall, PDMS was roll-imprinted until uniformly deposited on the SU-8 micro-wall (Figure S1C-i), after which additional PDMS was spin-coated on it (spin coat: 3000 rpm, 30

s) (Figure S1C-ii). Subsequently, the coated PDMS was baked at the target curing temperature (50 °C < $T' <$ 200 °C), which pre-determines the initial curvature of the SMF (Figure S1C-iii). The PDMS soaked in the SU-8 micro-wall showed strong adhesion, while the adhesion between PI and PDMS was low. Because of this phenomenon, the opening of the region for electrical contact was easily achieved by simply tearing the PDMS part (Figure S1D-i). With the simple tearing process, the PDMS that is not on the SU-8 micro-wall delaminates easily. Afterwards, the SMF was delaminated (Figure S1D-ii).

Demonstration of the shape morphing module

A convection oven was used for the demonstration of the shape morphing module because of the repeatable and accurate temperature difference required for different samples.

Characterization of the electrothermal heater

In this experiment, a 25×25 mm^2 heater was used. The calibration of IR camera was conducted prior to experimentation. The measured values from the thermocouple (midi LOGGER GL220 & ST-50, Graphtec Corporation & RKC Instruments, respectively, true value) and the measured value from the IR camera (E6, FLIR, calibration target) were compared for the same position on the electrothermal heater (Figure S5A). The temperature measured by the IR camera was higher than that of the thermocouple (Figure S5B). The cyclical heating-cooling experiment was performed using the thermocouple (Figure S5C), and the temperature just prior to power off was used as the stabilized temperature value for the analysis of the ΔT-P' relationship (Figure S5D). For the characterization of heating uniformity, the inner 20×20 mm^2 region of the heater was used, and the temperature of this region was extracted from the raw IR camera data. The extracted temperature was adjusted using the IR camera calibration result, and the average and standard deviations were analyzed.

Characterization of the SMF

For the sample used in the characterization, $T' = 100$ °C was adopted. The state of the SMF was controlled via P', and the R of each SMF was measured before the test to calculate the voltage needed for the target P'. The curvature for each P' was measured after 30 s of voltage onset. For the cyclic test, 200 cycles of heating/cooling were conducted using an electrical relay setup (**Figure S9**), and the first five cycles were analyzed. The electrical relay was controlled using LabView and NI-USB6211. Five sets of 200 cycles were conducted continuously, and the results were superimposed. Before starting cyclic test of the belt-shaped

SMF, aging was performed for 1000 cycles in which single cycle comprised heating of 15 s with $P' = 0.6$ [W/cm^2] and cooling of 15 s with $P' = 0$ [W/cm^2].

Artificial inchworm

To increase the morphing force of the artificial inchworm, $T' = 120$ °C was adopted for PDMS curing. After the fabrication of the SMF, a copper wire (AWG45) was soldered to the wiring of the artificial inchworm. Each voltage point (V_1–V_6) was controlled using an electrical relay setup (Figure S9). All motions were performed on a glass plate and recorded by an IR camera (ONE Pro iOS & iPhone XS, FLIR & Apple Inc. respectively) in the same direction as the optical camera in real time. For the morphing, $P' = 0.16$ [W/cm^2] was selected for the leg part, and $P' = 0.32$ [W/cm^2] for the foot part (with the same driving voltage).

Artificial Drosera Capensis

To fabricate the voltage line at both ends of the leaves, an insulator is required between the heater and the interconnection, because V_1 and V_4 should have the form of cilia. For artificial *Drosera Capensis*, $T' = 100$ °C was used for PDMS curing. For the "ready-to-catch" stage, $P' = 0.23$ [W/cm^2] of the power was initially applied, and sequentially stabilized at $P' = 0.17$ [W/cm^2]. After the artificial fly with a mass of 0.2 g was placed on the artificial *Drosera Capensis*, the voltage was turned off.

Supporting information

Calculation of the curvature from simulated result

Calculation of the theoretical turn factor

Figure S1. Detailed fabrication process of the SMF.

Figure S2. Details of the design optimization of the SU-8 micro-wall pattern and adjacent PDMS layer.

Figure S3. Overall optimization result ranked by curvature calculated from simulation for various conditions of the SU-8 micro-wall.

Figure S4. Characterization of the shape morphing module.

Figure S5. Characterization of the electrothermal heater.

Figure S6. Effect of aging on belt shape SMF.

Figure S7. Voltage profile for the movement of the artificial inchworm.

Figure S8. Characterization of the artificial inchworm motions.

Figure S9. Controller setup for the repetitive/multiple area control.

Table S1. Figure of merit for the comparison with related studies.

Movie S1. 1×1 square shape SMF.

Movie S2. 5×5 square shape SMF.

Movie S3. 4×52 belt shape SMF.

Movie S4. Front to back flip.

Movie S5. Back to front flip.

Movie S6. Crawl.

Movie S7. Left turn.

Movie S8. Right turn.

Movie S9. Drosera Capensis.

Received: ((will be filled in by the editorial staff))

Revised: ((will be filled in by the editorial staff))

Published online: ((will be filled in by the editorial staff))

References

[1]   J. Ahn, Y. Jeong, Z.-J. Zhao, S. Hwang, K. Kim, J. Ko, S. Jeon, J. Park, H. Kang, J.-H. Jeong, I. Park, *Adv. Mater. Technol.* **2020**, *5*, DOI 10.1002/admt.201900997.

[2]   H. Kim, H. Lee, I. Ha, J. Jung, P. Won, H. Cho, J. Yeo, S. Hong, S. Han, J. Kwon, K. J. Cho, S. H. Ko, *Adv. Funct. Mater.* **2018**, *28*, 1.

[3]   M. Amjadi, M. Sitti, *Adv. Sci.* **2018**, *5*, DOI 10.1002/advs.201800239.

[4]   Q. Wang, Y. T. Li, T. Y. Zhang, D. Y. Wang, Y. Tian, J. C. Yan, H. Tian, Y. Yang, F. Yang, T. L. Ren, *Appl. Phys. Lett.* **2018**, *112*, DOI 10.1063/1.5020918.

[5]   Z. Ren, W. Hu, X. Dong, M. Sitti, *Nat. Commun.* **2019**, *10*, DOI 10.1038/s41467-019-10549-7.

[6]   C. Wang, K. Sim, J. Chen, H. Kim, Z. Rao, Y. Li, W. Chen, J. Song, R. Verduzco, C. Yu, *Adv. Mater.* **2018**, *30*, 1.

[7]   Q. Li, C. Liu, Y. H. Lin, L. Liu, K. Jiang, S. Fan, *ACS Nano* **2015**, *9*, 409.

[8]   J. Zhang, Y. Guo, W. Hu, M. Sitti, *Adv. Mater.* **2021**, *33*, DOI 10.1002/adma.202100336.

[9]   M. Sang, G. Liu, S. Liu, Y. Wu, S. Xuan, S. Wang, S. Xuan, W. Jiang, X. Gong, *Chem. Eng. J.* **2021**, *414*, 128883.

[10]   S. Yao, J. Cui, Z. Cui, Y. Zhu, *Nanoscale* **2017**, *9*, 3797.

[11]   H. Lee, H. Kim, I. Ha, J. Jung, P. Won, H. Cho, J. Yeo, S. Hong, S. Han, J. Kwon, K.-J. J. Cho, S. H. Ko, *Soft Robot.* **2019**, *6*, 760.

[12]   Y. Xiao, J. Mao, Y. Shan, T. Yang, Z. Chen, F. Zhou, J. He, Y. Shen, J. Zhao, T. Li, Y. Luo, *Nanoscale* **2020**, *12*, 7514.

[13]   K. Yoonho, P. G. A., L. Shengduo, Z. Xuanhe, *Sci. Robot.* **2019**, *4*, eaax7329.

[14]   W. Hu, G. Z. Lum, M. Mastrangeli, M. Sitti, *Nature* **2018**, *554*, 81.

[15]   W. Wang, L. Yao, C.-Y. Cheng, T. Zhang, H. Atsumi, L. Wang, G. Wang, O. Anilionyte, H. Steiner, J. Ou, K. Zhou, C. Wawrousek, K. Petrecca, A. M. Belcher, R. Karnik, X. Zhao, D. I. C. Wang, H. Ishii, *Sci. Adv.* **2017**, *3*, e1601984.

[16]   H. Kim, S. kyun Ahn, D. M. Mackie, J. Kwon, S. H. Kim, C. Choi, Y. H. Moon, H. B. Lee, S. H. Ko, *Mater. Today* **2020**, *41*, 243.

[17]   N. Tanjeem, M. B. Minnis, R. C. Hayward, C. W. Shields, *Adv. Mater.* **2022**, *34*, 1.

[18]   Q. Li, X. Wang, L. Dong, C. Liu, S. Fan, *Soft Matter* **2019**, *15*, 9788.

[19]   Y. Wang, N. Wu, C. Liu, M. K. Albolkany, M. Wang, S. Arooj, W. Zhang, B. Liu, *Mater. Horizons* **2020**, *7*, 149.

[20]   B. Zuo, M. Wang, B. P. Lin, H. Yang, *Nat. Commun.* **2019**, *10*, DOI 10.1038/s41467-019-12583-x.

[21]   J. Li, L. Mou, R. Zhang, J. Sun, R. Wang, B. An, H. Chen, K. Inoue, R. Ovalle-Robles, Z. Liu, *Carbon N. Y.* **2019**, *148*, 487.

[22]   H. Qin, T. Zhang, N. Li, H. P. Cong, S. H. Yu, *Nat. Commun.* **2019**, *10*, 1.

[23]   J. Cui, T. Y. Huang, Z. Luo, P. Testa, H. Gu, X. Z. Chen, B. J. Nelson, L. J. Heyderman, *Nature* **2019**, *575*, 164.

[24]   Y. Zhu, M. Birla, K. R. Oldham, E. T. Filipov, *Adv. Funct. Mater.* **2020**, *30*, 1.

[25]   Y. Cao, J. Dong, *Soft Matter* **2021**, *17*, 2577.

[26]   S. Armon, E. Efrati, R. Kupferman, E. Sharon, *Science (80-.).* **2011**, *333*, 1726.

[27]   M. Schaffner, J. A. Faber, L. Pianegonda, P. A. Rühs, F. Coulter, A. R. Studart, *Nat. Commun.* **2018**, *9*, DOI 10.1038/s41467-018-03216-w.

[28]   G. M. Spinks, *Adv. Mater.* **2020**, *32*, 1.

[29]   H. Deng, C. Zhang, J. W. Su, Y. Xie, C. Zhang, J. Lin, *J. Mater. Chem. B* **2018**, *6*, 5415.

[30]   M. Ilami, H. Bagheri, R. Ahmed, E. O. Skowronek, H. Marvi, *Adv. Mater.* **2021**, *33*, 1.

[31]   A. Del Campo, C. Greiner, *J. Micromechanics Microengineering* **2007**, *17*, DOI 10.1088/0960-1317/17/6/R01.

[32]   F. Hartmann, L. Penkner, D. Danninger, N. Arnold, M. Kaltenbrunner, *Adv. Sci.* **2021**, *8*, 1.

[33]   Y. Jeong, H. jung Kang, Z. jun Zhao, J. Ahn, S. Hyoung Hwang, S. Jeon, J. Ko, J. Y. Jung, I. Park, J. ho Jeong, *Appl. Surf. Sci.* **2021**, *552*, 149500.

[34]   Myotis, "Inchworm," can be found under https://www.shutterstock.com/ko/image-photo/inchworms-walking-broken-branch-454946236**.**

[35]   E. Cooper, "D. Capensis," can be found under https://www.shutterstock.com/ko/image-photo/leaf-cape-sundew-plant-drosera-capensis-1986664298**.**
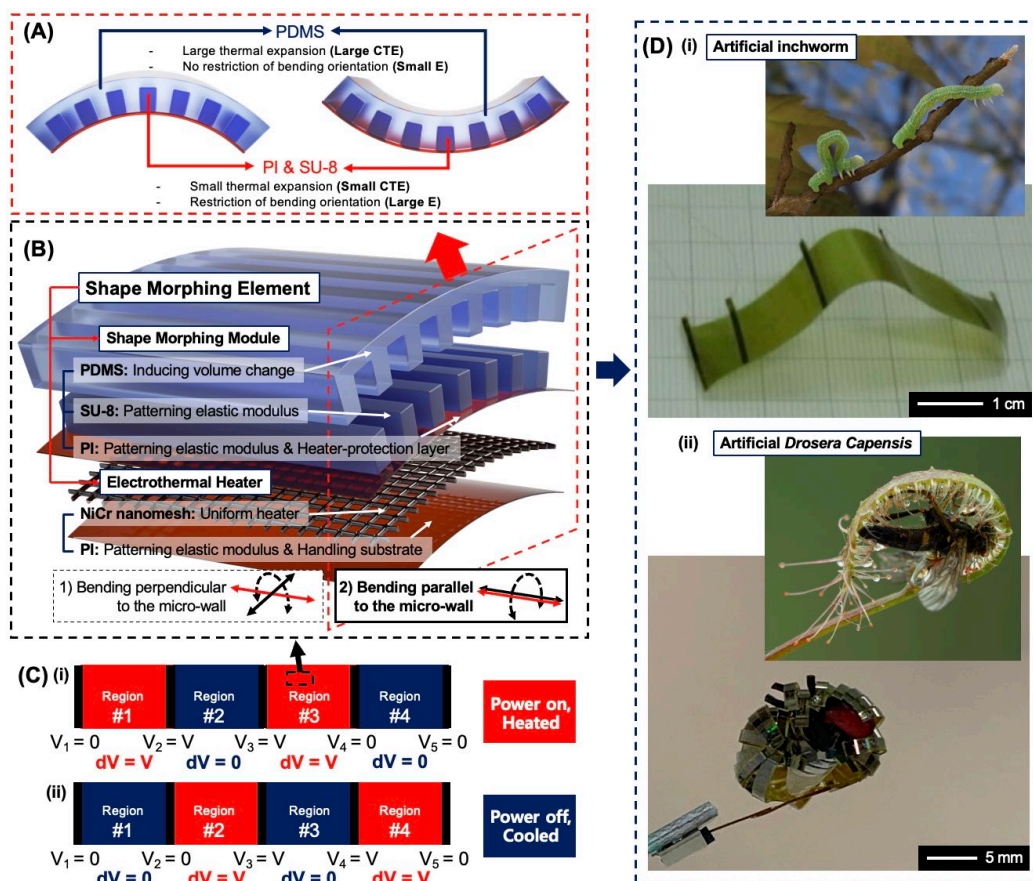
Figure 1. Schematic of the proposed biomimetic, programmable, and part-by-part maneuverable single-body shape morphing film. (A) Principle of the proposed shape morphing module. Due to the difference in the coefficient of thermal expansion (CTE) and elastic modulus (E) between materials, each material exhibits different morphological changes with temperature, resulting in the bending of the overall shape; (B) Exploded view of the proposed shape morphing film (SMF). SMF is composed of two parts: a shape morphing module (PDMS, SU-8 and PI) and electrothermal heater (NiCr nano-mesh based electrothermal heater and PI); (C) mechanism for the part-by-part maneuvering. When the voltages applied at two nodes are different, the area between these nodes is heated (red-colored region). On the other hand, when the voltages applied at two nodes are the same, the area between these nodes is not heated (right, blue-colored region). Two examples for the stepping-stone mode heating can be found in (i: heating of regions #1 and #3) and (ii: heating of regions #2 and #4); (D) Biomimetic applications using the proposed shape morphing module: The movements of the inchworm [34] (i) and *Drosera Capensis*[35] (ii) were adopted as examples of natural complex movements and performed using the proposed part-by-part maneuverable SMF.
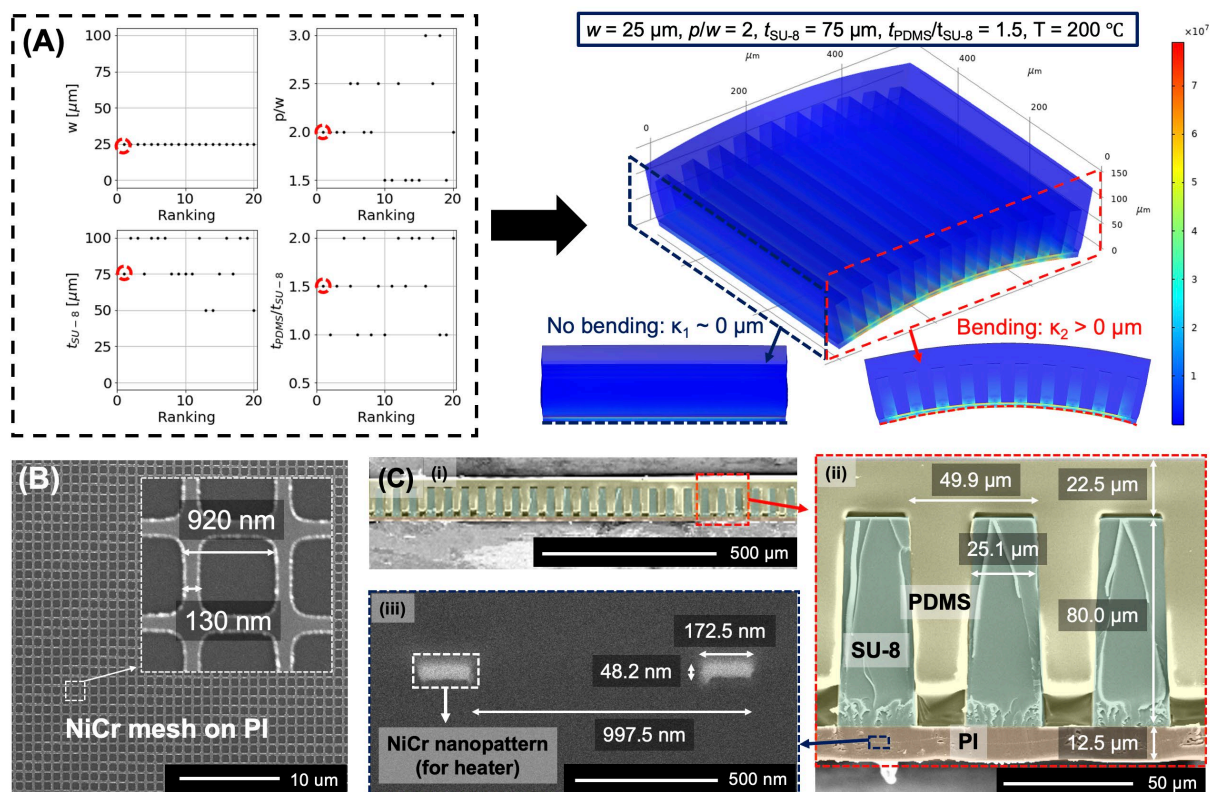
Figure 2. Optimization and fabrication of the shape morphing module. (A) The top 20 results from the simulation are shown on the left. "Ranking" describes curvature change, varying from none (low rank) to the greatest change (high rank). Optimal values for each variable are circled in red, and the corresponding condition is depicted on the right; (B) SEM image of the NiCr nano-mesh heater; (C) (i) Cross-sectional SEM image of the final product. It can be seen that (ii) the SU-8 micro-wall pattern and PDMS were fabricated as designed, and (iii) the NiCr nano-mesh heater is positioned between two PI layers.
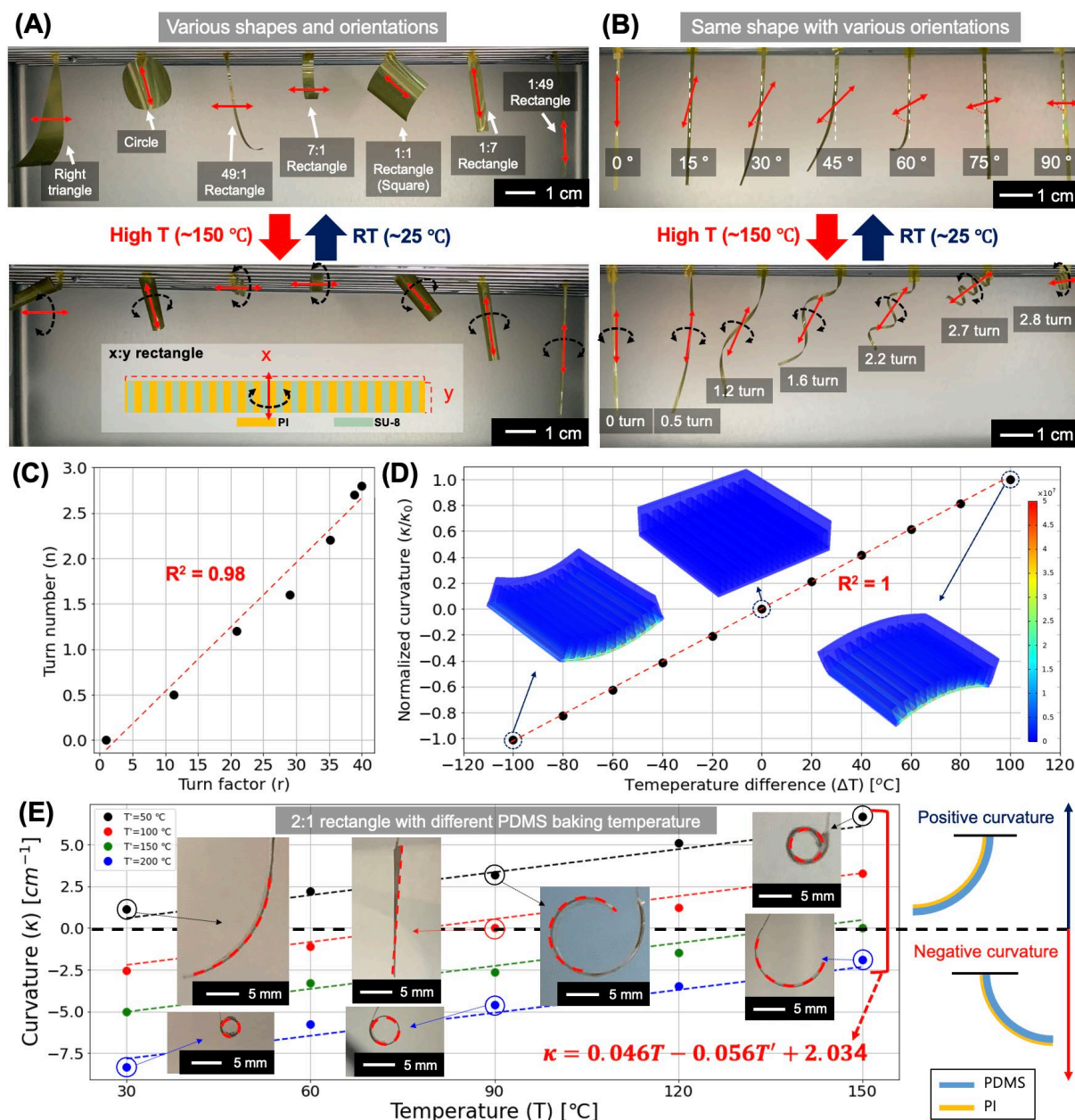
Figure 3. Confirmation of the programmability of the shape morphing module. (A) Characterization results of the shape morphing modules: Right-angle triangle, circle, and rectangles with various aspect ratios (49:1, 7:1, 1:1, 1:7, 1:49) were tested; (B) Results for the shape morphing modules with various orientations for the same SMF shape. A long belt-shaped shape morphing module was adopted in this experiment. The orientation was changed from parallel (0°) to perpendicular (90 °) to the belt direction, with an increment of 15°. The proposed module is seen to adopt its predesigned direction; (C) Linear relationship between the theoretical turn factor (r) and the real turn number (n); (D) Simulation result showing the linear relationship between the temperature change (ΔT) and the normalized curvature (κ/κ_{max}). (inset) Simulation results for the case of $\Delta T = -100, 0, 100$ ℃; (E) The linear

relationship between the curvature of the SMF (κ) and the PDMS curing temperature (T') and operating temperature of the shape morphing module (T).
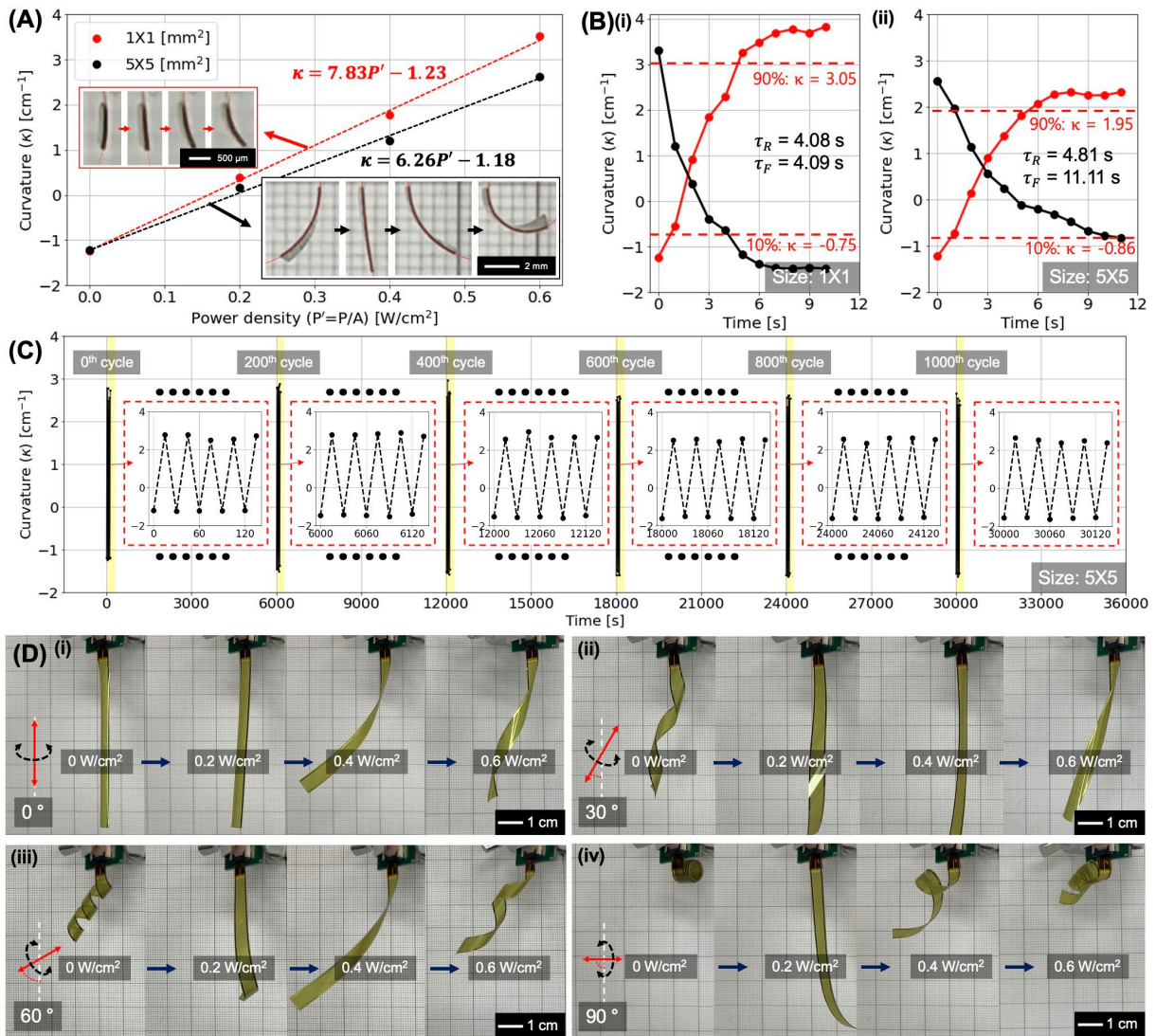
Figure 4. Characterization of the programmable SMF with various shapes. (A) $P' - \kappa$ relationship of the square shape SMF. Two sizes of square SMF (1×1 and 5×5 mm^2) were tested. The relationship was found to be linear with sensitivity of 7.83 and 6.26 [cm/W] for the 1 x 1 and 5 x 5 mm^2 square-shaped actuators, respectively. This result agrees well with the theoretical prediction ($\kappa \propto P' \propto \Delta T$); (B) Response time analysis for square shape SMF. Rise time (τ_R) and fall time (τ_F) were calculated as 4.08 s and 4.09 s for the 1×1 mm^2 square shape actuator, and 4.81 s and 11.11 s for the 5×5 mm^2 square shape actuator; (C) Cyclic test result of the 5×5 mm^2 module. Stable actuations of over 1000 cycles were confirmed; (D) The driving result for the belt shape SMF (size: 4×52 mm^2). For various bending orientations, the fabricated belt shape SMF followed the designed orientation well.
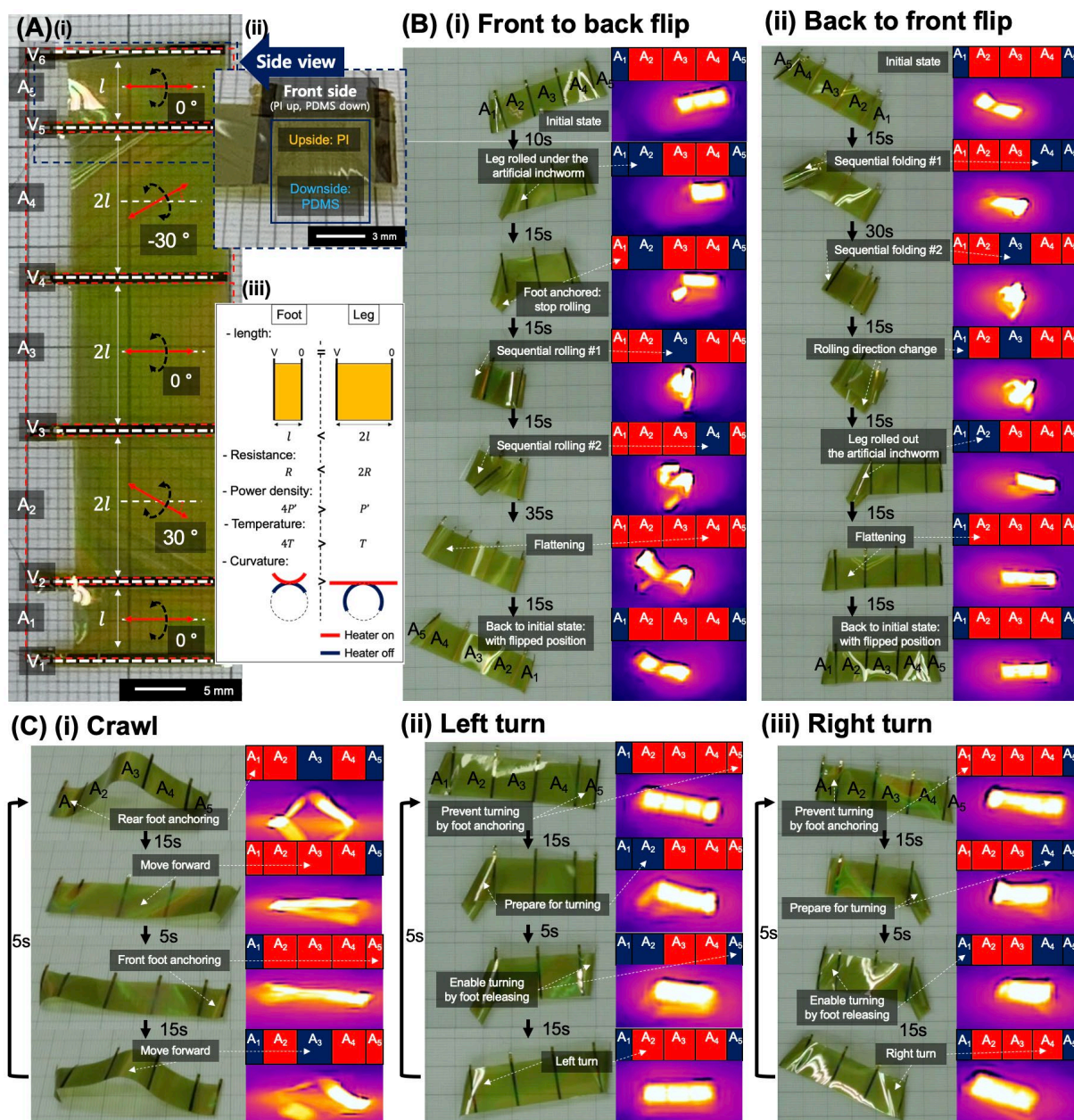
Figure 5. Applications of SMF in artificial inchworm. (A) (i) Fabricated artificial inchworm comprising foot (A_1, A_5) and leg (A_2-A_4) parts: A_1, A_3, and A_5 have identical morphing orientation (perpendicular to the length direction of the entire system), A_2 has a 30° slanted orientation with respect to that of A_3, and A_4 has a -30° slanted orientation with respect to that of A_3. (ii) To set the standard direction for movement, the front (PI side on top and PDMS side underneath) was set as shown. (iii) To adopt the bi-morph feature on the foot with same voltage level that flattens the legs, the feet were designed to have half the length of the legs, which resulted in a higher power density in the foot part. Due to the bi-morph feature, the foot selectively anchors (contact with PDMS side) and releases (contact with PI side) with the non-patterned flat glass ground; (B) Pose stabilization mechanism of the artificial inchworm: (i) front-to-back flip and (ii) back-to-front flip. While one side of leg

holds the stability of the overall film, the other side flips over or under the overall film, and this causes the flipping of the SMF. (C) Basic movement mechanisms of the artificial inchworm: (i) Crawling of the artificial inchworm and (ii-iii) turning of the artificial inchworm. For the crawling case, the overall film moves forward by repetitive bending of A_3, while movement direction is controlled by selective anchoring/releasing of each foot (A_1, A_5). In case of turning, the overall film turns by repetitive bending of the A_2/A_4 (left turn/right turn, respectively), while the turning direction is controlled by selective anchoring/ releasing of each foot (A_1, A_5).
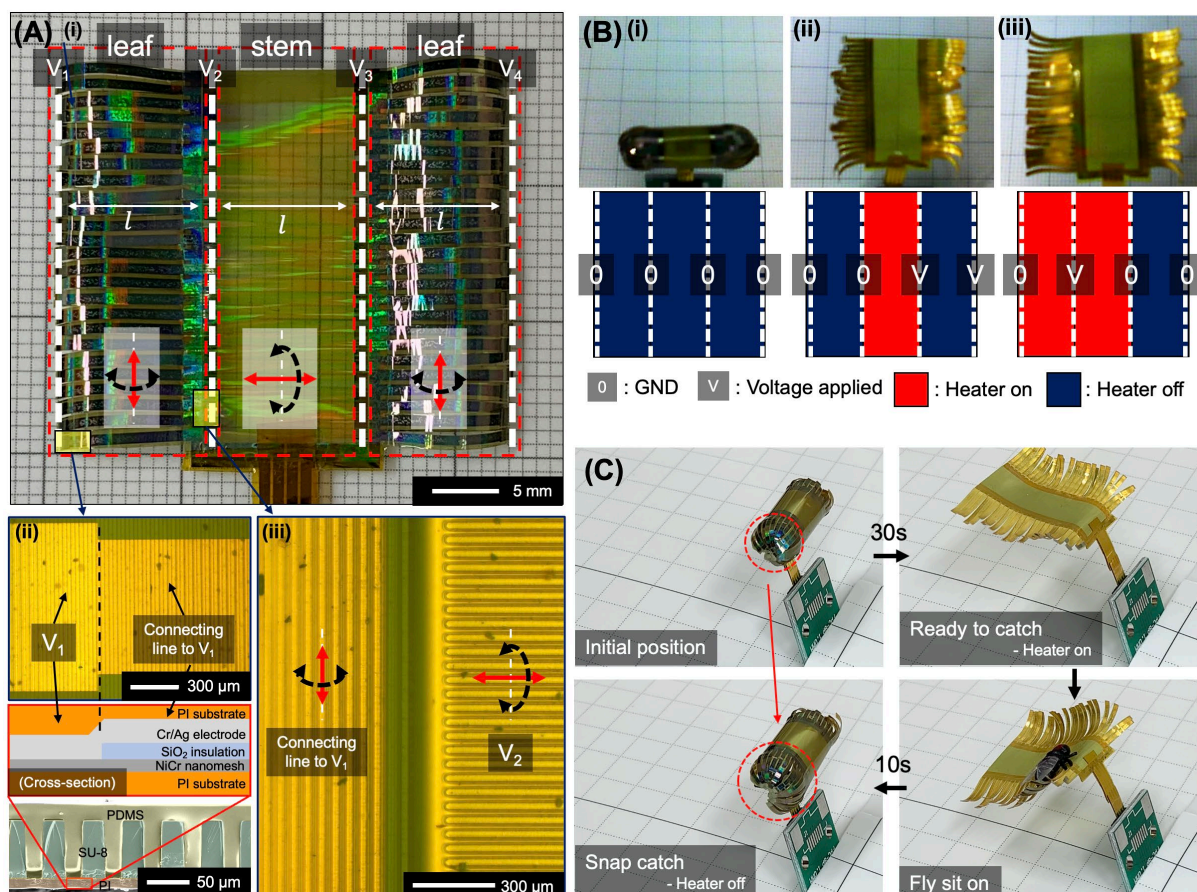
Figure 6. Application of SMF in artificial *Drosera Capensis*. (A) (i) Fabricated artificial *Drosera Capensis*. This comprises leaf and stem parts, which have mutually perpendicular morphing orientations. The leaf carries multiple cilia-like structures. (ii) Magnified view for the individual electrode (V_1) for cilia structure. For the electrical connection between V_1 and V_2 by only NiCr nanomesh, not the electrode film, the SiO_2 insulating layer was deposited between NiCr nanomesh and the electrode film layer. (iii) Magnified view for the boundary of the leaf and stem. At this boundary, the direction of the SU-8 microwall pattern is rotated by 90 ° to create a bending of the leaf perpendicular to that of the stem.; (B) Examples of part-by-part maneuvering of the artificial *Drosera Capensis*: (i) Heater was turned off for the whole SMF, and thus whole parts were rolled. (ii) Heater was turned on for the stem part, and thus it was unfurled while leaves were still rolled. (iii) Heater was turned on for the stem and left leaf, and thus they were unfurled while the right leaf was still rolled; (C) Movement of the *Drosera Capensis*. Since the electrode-to-electrode length of each actuator (l at Figure 6A) is the same, the power density P' is the same for the overall actuator at the same voltage difference, and achieves an equally flat position (at "ready to catch" state) despite the difference in the morphology of the stem and leaves.